

## 3D Reconstruction of virtual colon structures from colonoscopy images



DongHo Hong<sup>a</sup>, Wallapak Tavanapong<sup>a,\*</sup>, Johnny Wong<sup>a</sup>, JungHwan Oh<sup>b</sup>,  
Piet C. de Groen<sup>c</sup>

<sup>a</sup> Department of Computer Science, Iowa State University, Ames, IA 50011-1040, USA

<sup>b</sup> Department of Computer Science & Engineering, University of North Texas, Denton, TX 76203, USA

<sup>c</sup> Mayo Clinic College of Medicine, Mayo Clinic, Rochester, MN 55905, USA

### ARTICLE INFO

#### Article history:

Received 11 February 2013

Received in revised form 10 October 2013

Accepted 14 October 2013

#### Keywords:

3D Colon reconstruction

Optical colonoscopy

Virtual colon

Quality of colonoscopy

### ABSTRACT

This paper presents the first fully automated reconstruction technique of 3D virtual colon segments from individual colonoscopy images. It is the basis of new software applications that may offer great benefits for improving quality of care for colonoscopy patients. For example, a 3D map of the areas inspected and un-inspected during colonoscopy can be shown on request of the endoscopist during the procedure. The endoscopist may revisit the suggested un-inspected areas to reduce the chance of missing polyps that reside in these areas. The percentage of the colon surface seen by the endoscopist can be used as a coarse objective indicator of the quality of the procedure. The derived virtual colon models can be stored for post-procedure training of new endoscopists to teach navigation techniques that result in a higher level of procedure quality. Our technique does not require a prior CT scan of the colon or any global positioning device. Our experiments on endoscopy images of an Olympus synthetic colon model reveal encouraging results with small average reconstruction errors (4.1 mm for the fold depths and 12.1 mm for the fold circumferences).

© 2013 Elsevier Ltd. All rights reserved.

### 1. Introduction

Colorectal cancer is the second leading cause of cancer-related deaths behind lung cancer in the United States [1]. The survival rate is higher if the cancer is found and treated early before metastasis to lymph nodes or other organs occurs. Optical colonoscopy (OC), or colonoscopy, is currently the gold standard method for detection and prevention of colorectal cancer. Recent studies reported a low protective effect of colonoscopy against colorectal cancer, especially for the right colon (near 0%) [2,3]. Reports indicate the identity of the endoscopist performing the procedure as the dominant indicator of the protective effect of colonoscopy, not the withdrawal time [4,5]. The amount of colon mucosa inspected by the endoscopist is fundamentally important since the endoscopist cannot diagnose a problem (polyps, cancer, or other abnormal lesions) if the area where the problem resides is not seen in the first place. Domain experts estimate that under optimal conditions, inspection of around 90–95% of the colon mucosa during the withdrawal phase is possible and desirable [6]. The withdrawal phase starts when the

endoscopist reaches the most proximal part of the colon and begins to pull back the endoscope to carefully inspect the colon mucosa. A recent study estimated the amount of inspected colon mucosa of about 81%, much less than expected [7]. The study involved 65 screening colonoscopies under optimal conditions (i.e., patient age between 45 and 60 years, good or excellent colon preparation, no previous surgery of the colon, and evidence of ileocecal valve identification).

Standard endoscopes used in clinical practice are not equipped with any global positioning device to provide camera location and orientation or the colon structure. Current software does not indicate the mucosa areas inspected or how much of the colon mucosa is seen. Recent advances in endoscopy hardware include the following. (i) Avantis Third-eye retroscope that can be inserted into a working channel of an existing scope to enable the endoscopist to see the back of colon folds. (ii) Olympus Narrow Band Imaging, Fujinon Intelligent Color Enhancement, and Pentax Medical iScan that enable differences in colon mucosa and sub-mucosa to be seen easier. (iii) Invendo Medical invendoscopy that eases the advancement of the scope. None of the new hardware provides information about how well the colon mucosa is inspected during colonoscopy.

CT colonography (CTC) has been intensively studied. It constructs a virtual colon from cross-section CT images taken when a patient is in supine or prone positions. Radiologists determine

\* Corresponding author. Tel.: +1 515 294 2987; fax: +1 515 294 0258.

E-mail addresses: [hdh7905@gmail.com](mailto:hdh7905@gmail.com) (D. Hong), [tavanapo@cs.iastate.edu](mailto:tavanapo@cs.iastate.edu) (W. Tavanapong), [wong@cs.iastate.edu](mailto:wong@cs.iastate.edu) (J. Wong), [Junghwan.Oh@unt.edu](mailto:Junghwan.Oh@unt.edu) (J. Oh).

candidate polyps from CT images and the virtual colon. CTC creates a virtual colon that is freely floating in the abdomen. The shape of the colon in this case is restricted due to the size of the abdominal cavity and fixations of the colon via the mesentery.

Using a prior virtual colon constructed from CTC to accurately determine the uninspected colon areas during colonoscopy of the same colon will be very difficult. This is because the shape of the colon during CTC and OC is different. In OC, the shape of the colon is also restricted by the endoscope inside it. The colon is distended to insert the endoscope and to inspect the colon mucosa. Furthermore, the colon moves due to breathing, heart contractions, etc.

3D reconstruction of the colon structure from a sequence of colonoscopy images may provide the answer of how the colon is inspected during colonoscopy. We discuss a few possible applications below.

- For post-procedure quality control, the percentage of the inspected areas of the colon during the withdrawal phase may be used as one of the objective indicators of colonoscopy quality.
- For real-time quality assistance, a 3D map of the areas uninspected by the endoscopists may be marked on the virtual colon built from colonoscopy images. The map may be shown on demand such as when the endoscopist finishes inspection of a section of the colon (e.g., the right colon, the transverse colon, and the left colon). The endoscopist may use the map to guide a second inspection of that colon section, in particular areas not inspected. The software recalculates the cumulative uninspected areas and shows them on the map. The endoscopist may perform another inspection or proceed to the next section of the colon when good quality of inspection estimated by the software is achieved.
- For colonoscopy education, the virtual colons may be stored and later used as examples for novice endoscopists to learn different navigation techniques that result in different levels of quality of inspection.

Reconstruction of a generic 3D object from a single image is extremely difficult. However, endoscopic images of the inside of the tubular colon are not as generic as images we often experience in everyday life. We take advantage of the tubular nature of the colon in our design of the reconstruction algorithms.

Our first attempt [8] required manually extracted fold contour information (see Fig. 1(a)) as input. Since our purpose of the surface reconstruction is to estimate the mucosa area hidden from the endoscopist's view, we do not focus on rendering the surface with realistic colon texture nor abnormalities as in existing techniques for computer assisted surgery [9–11]. Fig. 1(b–d) show reconstruction results using manually drawn fold contours. The uninspected candidate areas are shown in green. Our first attempt received great interest from endoscopists during the Digestive Disease Week 2009 conference [12] and during individual visits to endoscopy clinics and centers. Fully automated 3D colon reconstruction is challenging due to the following.

- First, only partial edges of colon folds can be detected because parts of fold surface may be flat or hidden behind another colon fold. For instance, folds 1 and 2 in Fig. 1(a) show flat surface near the bottom of the image. Fold 4 is partially hidden since the colon is not a straight tube.
- Second, strong light reflection, blood vessels, stool, biopsy or therapeutic instruments, and polyps, can appear in the images, which can cause strong edges. We need to effectively identify and discard these noise edges.
- Third, mapping edge segments to colon folds is challenging and subjective since there is no precise ground truth. Consider mapping complex edge segments in Fig. 2(c) to fold contours in

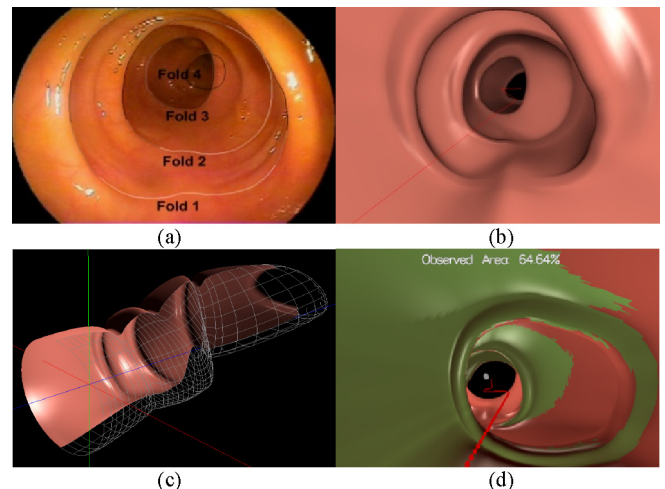


**Fig. 1.** (a) Input image with four colon fold contours manually labeled. (b) Front view of the virtual colon reconstructed from (a). (c) The reconstructed virtual colon segment with one side of the colon mucosa rendered showing overall structure. (d) Unseen mucosa area marked with green color, which is viewed backward from Fold 4 in (a) the small gray point indicates the position of the endoscope. The red line shows the colon center axis. (For interpretation of the references to color in this figure legend, the reader is referred to the web version of the article.)

**Fig. 2(d).** For instance, edge segment  $e_6$  in Fig. 2(c) has three candidate pairs in clockwise direction:  $e_2, e_7$ , and  $e_8$ .

- Fourth, the colon shape is not always circular. For instance, the transverse colon segment that goes across the body typically has triangular fold shapes.
- Finally, the colon is not rigid and can easily be deformed depending on the amount of air/ $\text{CO}_2$  used to inflate the colon. An effective reconstruction should correctly reconstruct the shape of the fold contours and place them in proper distances and alignment. The modeling of the colon fold surface and wall surface should take into account fold height (protrusion) and width (thickness).

In this work, we employ our previous work to automatically determine closed fold contours [13]. We propose *Depth-from-Intensity (DfI)* technique to estimate the distance of each fold from the camera using the brightness intensity of selected pixels around the fold contour. A single colon fold may have protruded parts and flat parts. The protruded part of the fold blocks light from the light source near the camera lens, causing large intensity difference between the pixels in front and behind the fold compared to that of the flat part. We use this intensity difference to estimate the fold height (protrusion) and width (thickness). Our final step is the generation of the colon surface using the estimated height and thickness in the interpolation method of fold surface as well as wall surface between neighboring fold contours and rendering the surface. The by-product of these algorithms is locational relation between the endoscope and the colon segment, which is used to compute the mucosa area that is out-of-view of the endoscope. The new technique does not require strong assumptions as in the previous technique [8].

Our contributions described in this paper are the DfI and the new algorithms for the colon surface and wall surface generation as outlined above. We evaluated our technique on twelve images obtained from the inside of an Olympus synthetic colon model. We measured fold distances and circumferences of folds in the colon model as ground truth and measured the average deviation of the fold depths and circumferences of the reconstructed colons compared to the ground truth. We provided examples of front and side views of the virtual colons reconstructed from real colonoscopy images to show that our technique can handle complexity of real

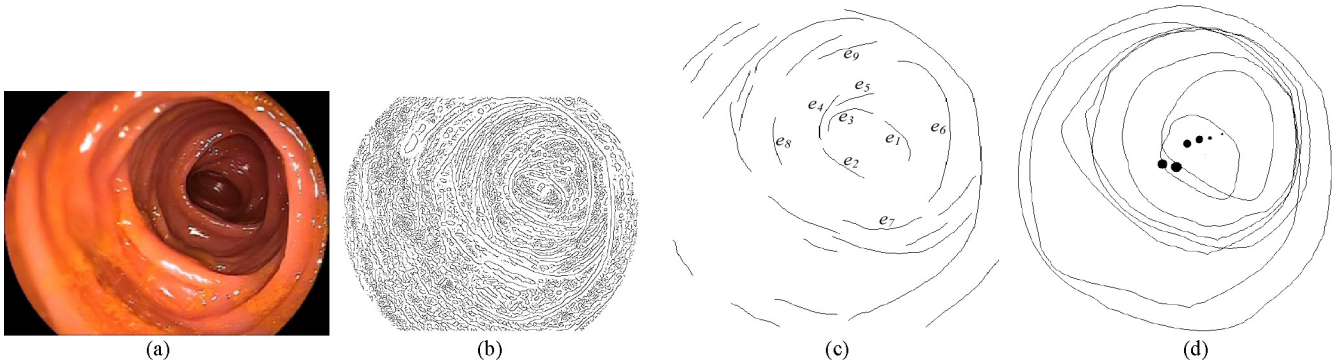


**Fig. 2.** (a) Complex colonoscopy image. (b) Result of Canny edge detection on (a) (c) remaining edges after noise filtering. (d) Completed colon fold contours; e1 and e3 are connected, forming the innermost fold contour. Edges e2, e4 and e6 are connected, forming the second innermost fold contour. e5 is effectively removed. The small dots are estimated centers of colon fold contours forming the colon center axis.

colonoscopy images. Since there is no actual ground truth on these real colons, we can only provide these examples as qualitative evaluation of the reconstructed results.

The remainder of this paper is organized as follows. Related work is summarized in Sections 2.1 and 2.2 followed by the summary of our previous work. Section 3.1 describes the new fold depth estimation algorithm, *Dfl*. Section 3.2 discusses our new colon surface generation algorithm and Section 3.3 provides an algorithm to estimate the uninspected mucosa area. The experimental method and results are reported in Section 4. Finally, we conclude the paper and give a description of future work in Section 5.

## 2. Related work

In this section, we first summarize recent work in CTC. Due to large amount of work in this field and limited space, we group them into major categories and reference recent publications in each category. Next, we discuss work in 3D reconstruction for generic objects. Finally, we provide background on our previous work on 3D reconstruction of colon structures.

### 2.1. Advances in CT colonography

- Automatic detection of polyps: polyps vary in shape, size, and complex surroundings. Example features investigated for automatic polyp detection are maximum, minimum, and mean of principal curvatures of surface [14], shape of vicinity of a voxel [15], 3D geometric features [16], and lines of curvatures [17]. Refs. [18,19] proposed methods to synchronize polyps seen between prone and supine positions to reduce false positives.
- Electronic colon cleansing: these methods automatically remove tagged stools from the reconstructed virtual colons. The major challenge is the partial volume effect where intensities of the interface between the air and the tagged stools overlap with those between the stools and the colon wall. Several techniques were proposed to address this issue using intensity profile, morphological and linear filters, and features of individual material classes (e.g., air, tagged stools, and colon wall) [20–23].
- Distortion-free colon flattening visualization [19,24] and a new navigation technique [25] using *Teniae coli* as anatomical references: *Teniae coli* are three parallel bands of longitudinal smooth muscles on the surface of the colon. They can be inferred from CTC-derived colonic surface as they are located anatomically at the edges of haustral folds and hastra.
- CTC-assisted optical colonoscopy [26,27]: These efforts attempt to utilize information obtained from CTC to assist the endoscopist during colonoscopy such as for locating polyps. The studies assume that the endoscope during colonoscopy follows

the shortest path and that the colon shape during CTC and colonoscopy are the same. They use discretized points on the centerline of a reconstructed virtual colon to find corresponding discretized points in the shortest path of the endoscope. The major challenges to bring the technology to clinical practice are as follows. (i) The colon shapes during supine and prone positions are significantly different from that during colonoscopy as mentioned above. And in colonoscopy the patient usually is most of the time in the left lateral position. (ii) The endoscope often does not follow the shortest path along the colon. For instance, the scope may form a loop, causing a significant mismatch between the location of the camera lens at the tip of the scope in the colon and the length of the inserted portion of the scope. (iii) The tip of the endoscope can be flipped around while the scope body is in the same position, causing different views of the colon wall.

### 2.2. Advances in 3D reconstruction of generic objects

Reconstruction of 3D models from 2D images is a challenging topic in computer vision and graphics communities. Existing approaches are *stereo-matching* [28,29], *shape-from-texture* [30], *shape-from-shading* [31,32], *shape-from-motion* [33], etc.

*Stereo-matching* calculates depth using disparity in appearance and location of features of a pair of images taken by different static cameras located on a same horizontal line with a constant distance apart from each other. Using two statically bounded cameras is ideal to achieve the above constraints. To simulate two cameras using a single moving camera, the camera motion must be predictable to maintain a geometrical relationship such as position and direction of the camera each time the image is taken. Because the movement of the camera is not predictable, stereo-matching is not suitable for reconstruction from endoscopy images. *Shape-from-texture* computes the shape of a surface from shapes of individual patterns on the surface with relatively same patterns. *Shape-from-texture* is not suitable for endoscopy images due to inconstant patterns of the colon wall.

*Shape-from-shading* (*SfS*) and *shape-from-motion* (*SfM*) are the two approaches that have been applied to endoscopy images. *SfS* computes the shape of a surface from the brightness of a single grayscale image of that surface. *SfM*, on the other hand, reconstructs the shape of an object surface from multiple sequential images. This approach consists of the following steps. First, prominent feature points of the object in these images are selected. Next, correspondence of the feature points across the images is established and the relative motion between the object and the camera is estimated. Finally, the 3D shape of the object surface is computed. A critical limitation of this approach is that the target object must be rigid. In

other words, the shape of an object must not be changed between the images.

Deguchi proposed a 3D colon surface reconstruction technique using *SfS* [9]. Koppel et al. [10] adopted *SfM* to reconstruct 3D colon surface and mapped texture from the input video on the reconstructed model. Kaufman et al. combined *SfS* and *SfM* [11]. Partial colon surface is reconstructed using the *SfS* algorithm that handles moving local light and light attenuation [31]. Then, with *SfM*, the camera motion parameters are estimated using features on the partial 3D surfaces created by the *SfS* algorithm. Finally, registration of these partial 3D surfaces (using these calculated extrinsic camera parameters) creates a more complete colon surface.

These existing works focus on colon surface reconstruction using *SfS* or *SfM*. These methods are not suitable to reconstruct tubular colon structure that indicates the alignment of colon folds, the distance among folds, the fold thickness, and the amount of fold protrusion. *SfS* would wrongly express lumen as a relatively far surface not a hole. *SfM* requires that the object be rigid, which is not the case for the human colon.

In Zhou et al. [34], an *optical-flow-based* method performs optical flow analysis to align neighboring 3D circles (not necessarily corresponding to colon folds) and determine the distance among them. The technique can generate a small 3D colon segment, but has the following limitations to reconstruct a realistic colon structure. First, some colon segments (e.g., transverse colon) may not be circular as assumed. Second, the technique assumes that the neighboring circles are not occluded; however, partial occlusion is typical. Third, the technique does not model colon fold thickness. Therefore, the mucosa behind thick folds may not be simulated.

### 2.3. Background on 3D reconstruction of a colon structure

The steps for reconstruction of a 3D virtual colon from a single endoscopic image are as follows.

1. Derive colon fold contours either manually [8] or automatically [13].
2. Perform reverse projection described in Section 2.3.2.
3. Determine the distance from the camera (depth) and the slant of the colon folds in 3D space using either our previous technique Depth-from-Shape (DfS) [8] or the proposed technique Depth-from-Intensity (DfI). DfS estimates the depth and the slant of a colon fold based on the assumption that a fold shape is close to a perfect circle, which is not the case in practice.
4. Use the colon fold contours in 3D space as the frame of the virtual colon structure. Generate the colon fold surface and wall surface between neighboring folds. Our previous technique [8] assumes that all folds have the same fixed fold width (thickness), which is not the case in practice. We relax this assumption in this proposed work.

#### 2.3.1. Fold contour estimation

Many existing image segmentation techniques are available in the literature. For instance, level set [35] and graph cut [36,37] methods may be modified for colon fold contour estimation to overcome the aforementioned challenges of noise, occlusion, and deformation of the colon. However, the modification is non-trivial, especially to handle occlusion. These techniques generally take significant time to generate region contours due to examination of pixel properties.

We proposed Iterative Geometric Region Expansion (IGRE) [13]. First, IGRE pre-processing obtains a set of candidate fold edges and the estimated center of the innermost fold. Next, IGRE assigns edges to colon folds iteratively starting from the innermost fold until all edges have been assigned. The criterion for the assignment is based on whether or not conditions for creation

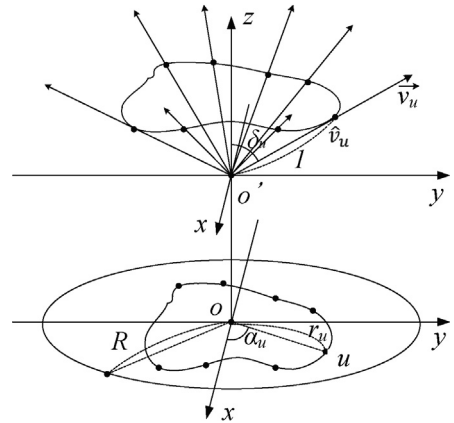


**Fig. 3.** Conversion of point  $u$  on a fold contour to reverse projection vector  $v_u$ .

of restriction lines representing missing edge segments between two real edge segments are satisfied. Once all edges that can be assigned to a current fold are assigned, a new center of the fold is calculated and the assigned edges are removed from further consideration. A Bézier curve [41] is drawn to bridge a small gap between edge segments. For a large gap, shape adoption is used. That is, the missing part of the innermost fold is estimated from shrinking the shape of its nearest outer fold after overlapping the center points of the two folds. We use a priority queue to keep two end point locations of each unassigned edge in our implementation. The priority is based on the distance of the end point to the current center of the fold. Hence, we do not need to examine pixel properties to group similar pixels into regions as in other region growing techniques. We evaluated the technique on 39 images from 7 colonoscopy video files. The ground truth determined manually and verified by de Groen indicates the presence or absence of folds and the contour of each fold in the image. **Results:** Average recall is 94.2%. Average precision is about 83% and the Mean  $\pm$  SD for the similarity metric is  $79.5 \pm 13.0$ . The similarity metric indicates the percentage of overlapping areas to the combined areas of the actual fold and the corresponding detected fold: the higher the value, the better the results. The contours and the associated properties are used as the input to the next step described in Section 3 to reconstruct a 3D virtual colon segment.

#### 2.3.2. Reverse projection

Reverse projection places fold contours in 3D space while correcting distortion caused by a fish-eye lens typically used in colonoscopes to allow for a wider field-of-view (FOV). The fish-eye lens uses one of these projection models: stereographic projection, equidistance projection, equisolid angle projection, or orthogonal projection [38,39]. We assume that the intrinsic parameters of the camera are given. That is, we know the projection model that the camera lens of the endoscope obeys.

Fig. 3 shows that for each point  $u$  in a 2D image (the bottom part of Fig. 3), there is a corresponding vector  $\vec{v}_u$  from the origin in the 3D coordinate. See the top part of Fig. 3. Given the projection model, we trace the ray projected on the image back in 3D space by first converting each pixel  $u$  on the fold contour to a unit vector of  $\vec{v}_u$  denoted as  $\hat{v}_u$  in 3D space. Given this unit vector, we obtain the corresponding reverse projection vector  $\vec{v}_u$ , once we estimate  $d_u$ , the distance of the pixel  $u$  from the camera, using either our previous DfS or our new DfI method as shown in Eq. (1).

$$\vec{v}_u = \hat{v}_u \cdot d_u \quad (1)$$

Let  $\delta_u$  be the angle between  $\hat{v}_u$  and the z-axis. Let  $x(\cdot)$  and  $y(\cdot)$  and  $z(\cdot)$  be the functions that give the x-coordinate, y-coordinate, and

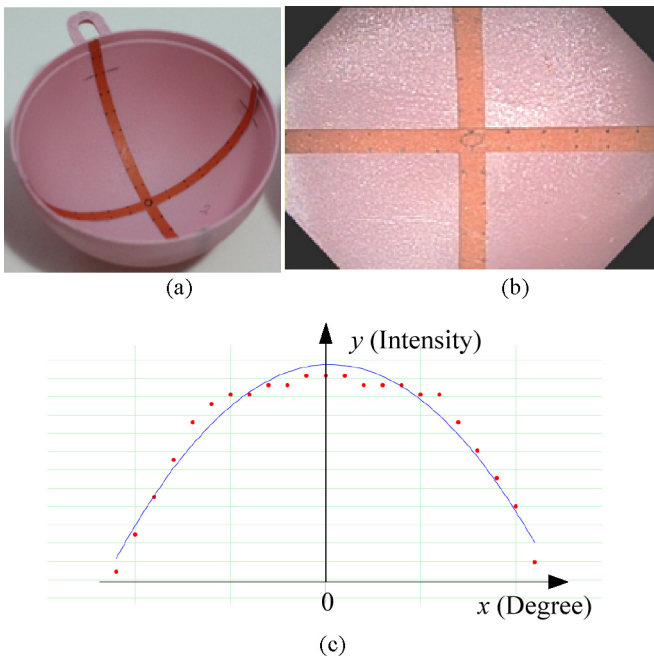


**Fig. 4.** (a) Hemisphere object marked with 18 scales at 10° apart. This object is used for measuring intensity distribution of the camera. (b) Image of the hemisphere object captured using Olympus PCF-H180AL with 140° FOV. (c) Dots show intensity values sampled along the horizontal line from (b). The purple line was the result of the polynomial regression fitting, which yields Eq. (2). (For interpretation of the references to color in this figure legend, the reader is referred to the web version of the article.)

*z*-coordinate, respectively. We know the values of  $x(u)$  and  $y(u)$ , we can compute the  $x$ ,  $y$ , and  $z$  coordinates of  $\hat{v}_u$ , as  $x(\hat{v}_u) = x(u)\sin\delta_u/r_u$ ,  $y(\hat{v}_u) = y(u)\sin\delta_u/r_u$ , and  $z(\hat{v}_u) = \cos\delta_u$  where  $r_u$  be the Euclidean distance of the point  $u$  from the image center  $o$ . Assuming that the camera has the equidistance projection, we have  $\delta_u = 0.5^*\text{FOV}^*r_u/R$ , where  $R$  is the image radius (see Fig. 3) which is the maximum value of  $r_u$ . A typical FOV for colonoscopes is 140°. More details on reverse projection can be found in Ref. [8].

### 3. Proposed work: colon reconstruction from intensity

Our proposed work consists of two major steps: depth estimation from intensity ( $DfI$ ) and colon surface generation.

#### 3.1. Depth estimation from intensity

Our depth estimation consists of two key steps: brightness intensity calibration and estimation of depth of each non-specular pixel based on its brightness intensity.

##### 3.1.1. Brightness intensity calibration

Brightness intensity calibration should be performed before we use pixel intensity to estimate distance of pixels from the endoscope. The rationale is that rays from the light source are more concentrated on the center of the image than the border of the image. We made a calibration object, a hemisphere with scales inside as shown in Fig. 4(a). The hemisphere object has a property that when a camera is placed at the center of the sphere, the distance from the camera to any point on the surface is identical. Furthermore, any point on the surface has its surface normal directing toward the camera. Thus, if the light source emits photons evenly around the surface, brightness intensity must be identical for all pixels.

We performed experiments by placing several types of endoscope such as Olympus CF-H180AL scope at the center of the sphere of the calibration object. We selected pixels near the stripe at the scale locations from the image shown in Fig. 4(b) to study the relation between the pixel brightness intensity and the degrees. These pixels are not specular pixels. As shown in Fig. 4(b), pixels near the center (0° in Fig. 4(c)) are brighter than pixels near the border. We obtained Equation (2) that predicts the intensity value  $y$  ( $0 \leq y \leq 255$ ) given a degree  $x$  using polynomial regression fitting [40].

$$y = -0.0168x^2 + 186 \quad (2)$$

Based on the above experiments, before calculation of pixel depth for each pixel involved in the calculation, we adjust the brightness intensity of the pixel based on the value of  $x$ , which is the degree calculated as  $\text{FoV} \times d/\text{imgw}$ . The value of  $d$  is the Euclidean distance of the pixel coordinate from the image center and  $\text{imgw}$  represents the image width. The adjusted intensity  $i'$  is obtained from the original pixel intensity  $i$  using Eq. (3) where  $0 \leq i$  and  $i' \leq 255$ .

$$i' = i + 0.0168x^2 \quad (3)$$

The adjusted brightness intensity is used in subsequent steps. We demonstrate the impact of the brightness intensity calibration on the reconstruction in Section 4.1.3.

#### 3.1.2. Depth-from-Intensity ( $DfI$ ) of non-specular pixels on a contour

We use brightness intensity of the surface around a fold contour to infer the distance of that surface from the camera. For estimation of depth from brightness intensity, the colon surface is assumed Lambertian except at specular spots. This assumption is also used in previous work for colon surface reconstruction for computer-aided surgery [11]. Under the assumptions that (i) a point light source and the camera lens are located at the same position and (ii) there is no ambient light, the Lambertian's cosine law in Eq. (4) holds.

$$i = \frac{C \cdot \cos\theta}{d^2} \quad (4)$$

where  $i$  is the intensity value;  $d$  is the distance between the camera and the surface;  $\theta$  is the slant angle between the observer's line of sight and the surface normal; and  $C$  is a constant representing an intrinsic camera property. Given the same slant angle, the surface at a further distance appears darker in the image than the surface closer to the camera. Given the same distance from the camera, the surface that slants more appears darker than the surface that slants less.

The assumption (ii), however, does not hold in practice since the closed structure of the colon and glossy mucosa cause significant ambient light. We performed experiments to explore the relationship between the brightness intensity and the distance from the camera in the colon by inserting a special ruler designed for colonoscopy as shown in Fig. 5(a). The deeper the surface is, the more effect the ambient light becomes as shown in Fig. 5(b). From our observation, the ambient light causes a slower drop in brightness intensity as the distance  $d$  increases than that described by Equation (4). We experimented with different values of the power coefficient  $m$  (0.5, 0.75, 1, 1.25, and 2) in Eq. (5). The detailed results are reported in Section 4. In summary, we found that  $m = 1$  gives the least estimation error from the ground truth measurements of an Olympus synthetic colon model.

$$i = \frac{C \cdot \cos\theta}{d^m} \quad (5)$$

Eq. (5) does not take the amount of protrusion of colon folds into account. For example, as shown in Fig. 5(c), tall folds block reflected lights from reaching inside, reducing the amount of ambient light

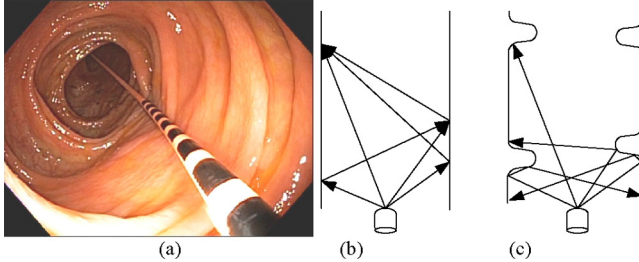


**Fig. 5.** (a) Experiment to establish the relation between the brightness intensity on a surface and the distance from the endoscope to the surface. (b) Colon surface is glossy, which reflects more light to the reflection angle and generates considerable ambient light. (c) Protruded folds blocks ambient light from deep surface.

on the surface whereas flat surface should result in more ambient light. For simplicity, we use Eq. (5) with  $m = 1$  hereafter.

Next, we estimate the depth (distance from the camera)  $d_u$  for every point  $v_u$  (in 3D space) corresponding to the pixel  $u$  on each of the fold contours. Let  $\theta_u$  be the slant angle of the surface normal at the point  $v_u$  and the line of sight of the camera. Each pixel  $u$  has corresponding brightness intensity denoted as  $i_u$ . We rearrange Eq. (5) and replace the parameters  $d$  and  $i$  with the parameters corresponding to the point  $u$ . Hence, we have Eq. (6).

$$d_u = \frac{C \cdot \cos \theta_u}{i_u} \quad (6)$$

To minimize the estimation error of  $d_u$ , we want to find a point close to  $u$  that best minimizes the slant angle  $\theta_u$ . When  $\theta_u = 0^\circ$  (the surface normal at this point faces directly to the line of sight of the camera),  $\cos 0^\circ = 1$ . However, we cannot use specular pixels since they do not obey the Lambertian's cosine law. Therefore, we find a suitable non-specular pixel close to the point  $u$ . According to the Lambertian's cosine law, for points located at the same distance from the camera, those appear brighter in the image have smaller slant angles. Hence, we search for the brightest non-specular pixel within a 1D window of size  $K$  starting from  $u$  along the normal direction of  $u$  away from the estimated center of the fold. The center is obtained by the fold contour estimation step (Section 2.2.1). We denote this brightest non-specular pixel  $u'$  and its intensity as  $i_{u'}$ . We estimate  $\theta_{u'}$  instead of  $\theta_u$ . To detect a specular pixel, we slide a square window (of size  $B \times B$  pixels) centered at each pixel in the image. If the intensity of the center pixel is  $T$  times higher than the average brightness intensity in the sliding window, the pixel is considered a specular pixel;  $T > 1$ . Fig. 6 illustrates key factors involved in the estimation. The green dots in Fig. 6(a) are examples of the brightest non-specular pixels along the fold contours.

Let  $w_u$  be a normalized distance (normalized by  $K$ ) between the contour pixel  $u$  and the corresponding brightest non-specular pixel  $u'$ ;  $0 < w_u \leq 1$ . For the point  $u$  where  $0 < w_u < 1$  (like Parts 1 and 2 in Fig. 6(b)), we set  $\theta_{u'}$  to  $0^\circ$  since the slant angle of the brightest non-specular pixel  $u'$  is closest to  $0^\circ$ . For the point  $u$  where  $w_u$  is 1, the brightest non-specular pixel  $u'$  is located outside the search range or this part of the fold may be flat (e.g., Part 3 of Fig. 6(b)). In this case, we consider the protrusion of the fold (height) in our depth estimation. Thus, we use Eq. (7) to represent the two cases.

$$d_u = \frac{C(\bar{w}_u \cdot \cos 0 + w_u \cdot \cos \theta_{u'})}{i_{u'}} \quad (7)$$

where  $\bar{w}_u = 1 - w_u$ . When  $w_u < 1$ ,  $d_u$  becomes  $C/i_{u'}$ . When  $w_u$  is 1, we consider the fold height at the point  $u$ . This fold height is estimated by  $h_u$  as the absolute difference of the average intensities of  $K$  pixels inside and  $K$  pixels outside of the contour along the perpendicular line across the pixel  $u$ . The more protruded fold blocks more rays of light from the light source near the camera. As a result, we see larger brightness difference between the pixels in front of

the fold and behind the fold. The value of  $h_u$  is normalized between 0 and 1 inclusive.

Let  $\theta_u^*$  be the slant angle when the fold at the point  $u$  is perfectly flat (i.e.,  $h_u$  is zero). When the fold at the point  $u$  is at the maximum height, we set  $\theta_{u'}$  to  $0^\circ$  since surface of tall folds faces the camera directly. The value of  $\theta_{u'}$  increases as the normalized height decreases. Thus, we have Eq. (8).

$$\theta_{u'} = \theta_u^* \cdot (1 - h_u) \quad (8)$$

The angle  $\theta_u^*$  at the flat surface point  $u$  can be estimated using the vector  $v_u$  and vector  $c$  from the camera to the contour center in 3D space as shown in Fig. 6(c). Finally, we have Eq. (9).

$$d_u = \frac{C(\bar{w}_u + w_u \cos(\arcsin(\hat{v}_u \cdot \hat{c})(1 - h_u)))}{i_{u'}} \quad (9)$$

Since we have  $d_u$ , we can obtain various points on the reverse-projected fold contours using Eq. (1) as shown in Fig. 6(d). These points scatter due to estimation errors of  $d_u$ . Moreover,  $d_u$  is not available for a point  $u$  in an occluded portion of a fold contour. To address these issues, we first remove outlier points using statistical boxplots. We found boxplots to be sufficiently effective for most fold contours, except the innermost contour, which is difficult to estimate correctly due to occlusion. Then, we fit the remaining points to a plane using the least squares fitting algorithm. This plane becomes the plane the fold is laid on. Then, we recalculate  $v_u$  by computing the cross point between  $\hat{v}_u$  and the plane for each point  $u$ . The values of constants  $C$ ,  $T$ ,  $B$  and  $K$  were determined experimentally as explained in Section 4.

### 3.2. Colon surface generation

There are two major types of surface: (i) surface of folds and (ii) surface between folds (or wall surface). We use Cubic Bézier curves [41] for interpolation of the surface. In our previous technique [8], we calculate the curves using a fixed fold width, which causes all folds to have same thickness (width), which is not the case for real colon folds. Furthermore, we did not consider smooth continuation of the surface among neighboring folds, which results in unnecessary protrusion in the reconstructed colon as shown in the left side of the image in Fig. 7(c). We propose a new method that uses several features extracted from an input colonoscopy image and geometrical relations between neighboring folds estimated in Section 3.1.2 to improve our previous surface generation technique.

We sample  $P$  evenly distributed points from each fold contour and assign indices to these points starting from the topmost point (the one with the biggest  $y$  coordinate) in the clockwise direction. The value of  $P$  is based on experiments shown in Section 4. The interpolation for surface is applied on corresponding points with the same index on different fold contours. Since the same algorithm is applied to each point, we omit the point index from the notations used in the rest of the description.

Fig. 8 shows the fold surface on  $p_{i0}$ , one of the sampled points on the  $i$ th fold contour. The corresponding surface generated from this point consists of a Bezier curve  $p_{i0}p'_{i2}$  on its left and another Bezier curve  $p_{i0}p_{i2}$  on its right. Another Bezier curve  $p_{i2}p'_{(i+1)2}$  expresses the wall surface,  $Wall\ i$ , between the  $i$ th fold and  $(i+1)$ th fold. The positions of  $p_{i2}$  and  $p'_{i2}$  are important and should be computed based on the estimated fold width and height in order to generate the surface that closely reflects the real surface. Thus, we use  $W_i$  and  $H_i$  computed as  $W \cdot w_u$  and  $H \cdot h_u$ , respectively where  $w_u$  and  $h_u$  are measured in the previous section. Recall that  $0 < w_u \leq 1$  and  $0 \leq h_u \leq 1$ . The constants  $W$  and  $H$  are the maximum fold width and fold height determined based on experiments in Section 4. Let  $q_i$

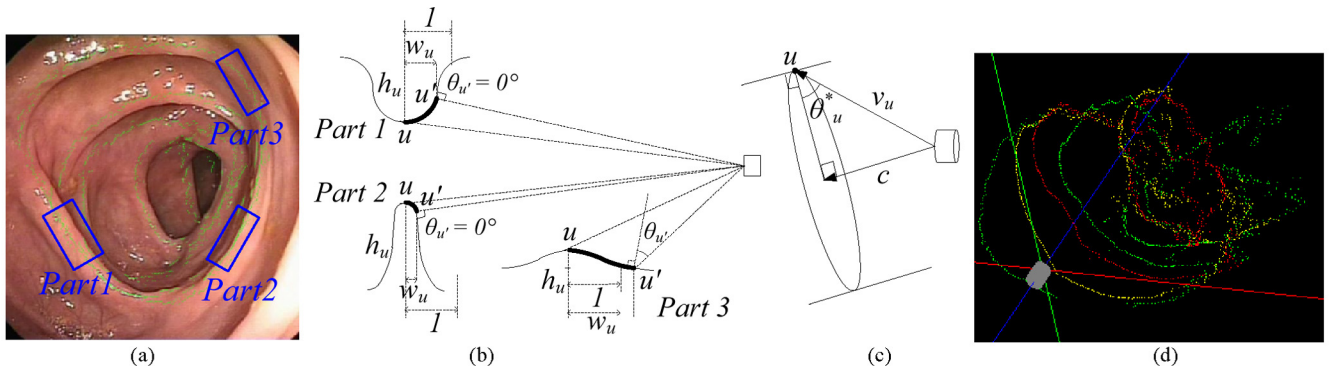


**Fig. 6.** (a) Blue rectangles mark different surface properties of a fold. The green dots represent the brightest non-specular pixels ( $u'$ ), within the 1D search window from the fold contours. (b) We estimate the value of  $\theta_u$  of part 1 and part 2 to be  $0^\circ$  as  $u'$  faces directly to the camera. However,  $\theta_u$  of part 3 cannot simply be set to zero since it depends on the fold protrusion. (c) For a wide fold like part 3, we estimate the value of  $\theta_u$  proportionally to the value of  $\theta_{u'}$ . Vector  $c$  is from the endoscope to the center of the fold contour. Vector  $v_u$  is the reverse projection of pixel  $u$ . We know the angle between  $c$  and  $v_u$ , and thus can calculate the value of  $\theta_u^*$ . (d) Scattered dots are the projections of the green dots in (a) on 3D space by  $DfI$ . Different color indicates different fold contours. (For interpretation of the references to color in this figure legend, the reader is referred to the web version of the article.)

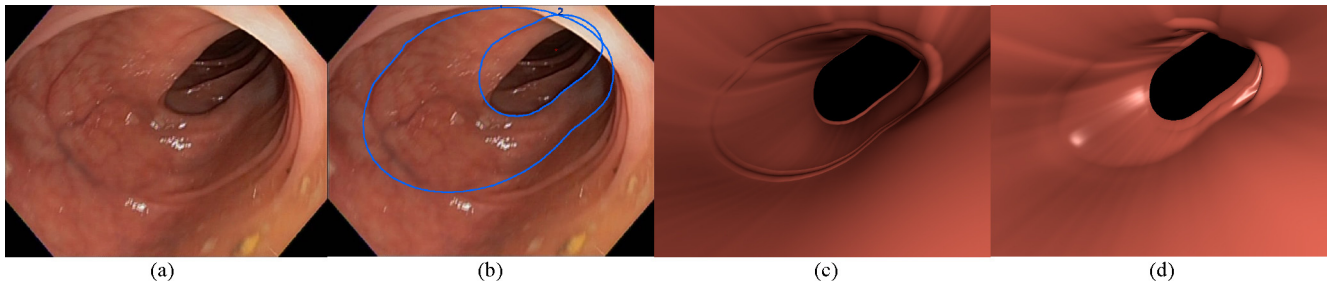


**Fig. 7.** (a) Original input image with flat surface on the left side. (b) Original image superimposed with the detected fold contours shown as blue lines. (c) Front view of the reconstructed colon segment using our previous technique shows unnecessary protrusion on the left side of the fold closest to the camera; however, the original image (a) shows flat surface. (d) Front view of the reconstructed colon segment using the proposed technique with a better expression for the flat part of the fold.

denote the center of the fold contour  $i$  in 3D space. We compute the positions of  $p_{i0}$  and  $p'_{i0}$  using Eqs. (10)–(14).

$$\vec{v}_{i0} = \overrightarrow{q_i p_{i0}} \quad (10)$$

$$\vec{v}_{i1} = \overrightarrow{p_{(i-1)0} p_{(i+1)0}} \quad (11)$$

$$p_{i1} = p_{i0} + H_i \cdot \hat{v}_{i0} \quad (12)$$

$$p_{i2} = p_{i1} + W_i \cdot \hat{v}_{i1} \quad (13)$$

$$p'_{i2} = p_{i1} - W_i \cdot \hat{v}_{i1} \quad (14)$$

Eq. (11) gives the vector that aligns the left and right neighboring folds of the fold  $i$ . Fig. 8 shows  $\vec{v}_{i1}$  twice parallel to each other for ease of understanding of Eqs. (12)–(14). We use Eqs. (12)–(14) to position the points  $p_{i2}$  and  $p'_{i2}$  on this vector  $\vec{v}_{i1}$  so that the three folds

align well and the fold width and height are taken into account. For a fold  $i$  which does not have the previous  $(i-1)$  or the next  $(i+1)$  fold, we use  $p_i$  instead of nonexistent  $p_{(i-1)}$  or  $p_{(i+1)}$  to calculate  $\vec{v}_{i1}$ .

Besides the two end points, each Cubic Bezier curve requires two control points to describe the shape of the curve. We need two control points,  $c_{i1}$  and  $c_{i2}$ , for the curve  $p_{i0}p_{i2}$  as shown in Fig. 9(a). For curve  $p_{i0}p'_{(i+1)2}$  connecting the  $i$ th and  $(i+1)^{th}$  folds, we need two more control points,  $c_{i3}$  and  $c'_{(i+1)3}$  as shown in Fig. 9(b). The positions of the control points are also important as they contribute to the shape of the Bezier curve. The control points  $c_{i1}$ ,  $c_{i2}$  and  $c_{i3}$  are calculated using Eqs. (15)–(20).

$$c_{i1} = p_{i0} + C_1 W_i \cdot \hat{v}_{i2} \quad (15)$$

$$p_{i3} = p_{i0} + C_2 H_i \cdot \hat{v}_{i0} \quad (16)$$

$$\vec{v}_{i3} = \overrightarrow{p_{i2} p_{(i+1)3}} \quad (17)$$

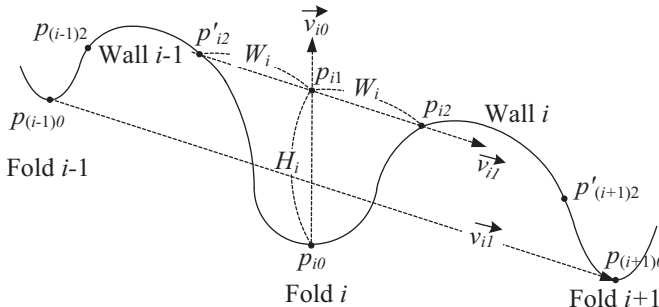


**Fig. 8.** Diagram showing an interpolation of the fold surface of fold  $i$ .

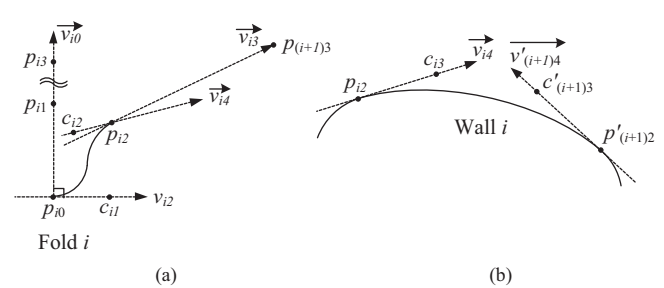


**Fig. 9.** Diagram demonstrating the interpolation of the wall surface of wall  $i$ . (a) Fold surface generation. (b) Wall surface generation.

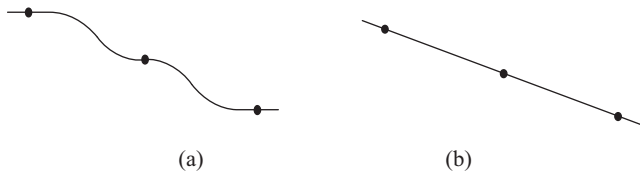


**Fig. 10.** (a) Expression for a flat portion of a fold with our old surface generation algorithm. (b) Expression for a flat portion of a fold with proposed new surface generation algorithm. Dots in (a) and (b) represent three consecutive folds.

$$\vec{v}_{i4} = \vec{v}_{i1} \cdot (1 - h_i) + \vec{v}_{i3} \cdot h_i \quad (18)$$

$$c_{i2} = p_{i2} - C_3 W_i \cdot \hat{v}_{i4} \quad (19)$$

$$c_{i3} = p_{i2} + C_4 \left| \overrightarrow{p_{i2}p'_{(i+1)2}} \right| \cdot \hat{v}_{i4} \quad (20)$$

Let  $C_1, C_2, C_3$ , and  $C_4$  be constants. The control point  $c_{i1}$  is set to be at a distance proportional to the width of the fold  $i$  on  $\vec{v}_{i2}$  – the vector perpendicular to  $\vec{v}_{i0}$ , as shown in Eq. (15). To set the positions of  $c_{i2}$  and  $c_{i3}$ , we calculate the position of the point  $p_{(i+1)3}$  using Eq. (16) but for the  $(i+1)$ th fold, instead of the  $i$ th fold. This point is on the normal vector of the corresponding point on the next fold  $p_{(i+1)0}$  at the distance proportional to the height of the fold. The vector  $\vec{v}_{i3}$  is computed using Eq. (17) to ensure a smooth connection of the wall surface between the two neighboring folds. Control points  $c_{i2}$  and  $c_{i3}$  are on vector  $\vec{v}_{i4}$  which is linearly interpolated between vectors  $\vec{v}_{i1}$  and  $\vec{v}_{i3}$  by the height of fold  $i$  using Eq. (18). The vector  $\vec{v}_{i4}$  of a flatter fold  $i$  ( $h_i$  is closer to 0), should be closer to  $\vec{v}_{i1}$  than  $\vec{v}_{i3}$  and vice versa. We select  $\vec{v}_{i4}$  this way to avoid unnecessarily protrusion when the fold is flat as shown in Figs. 10(b) and 7(d). Our previous surface generation algorithm resulted in unnecessary bumps as shown in Figs. 10(a) and 7(c). We place  $c_{i2}$  using Eq. (19) on  $\vec{v}_{i4}$  at the distance proportional to the width of the fold. By Eq. (20),  $c_{i3}$  is placed on  $\vec{v}_{i4}$  at the distance proportional to the distance between  $p_{i2}$  and  $p'_{(i+1)2}$ . Control points  $c_{i2}$  and  $c_{i3}$  on a same vector  $\vec{v}_{i4}$  make the curve at  $p_{i2}$  smooth. Control points  $c'_{i1}, c'_{i2}$  and  $c'_{i3}$  can be obtained similarly. Due to noise within an image and estimation errors, some portion of consecutive folds may conflict with each other. In this case, we adjust the slant of the farther of the conflicting folds as follows. We iteratively increase the depth of the invading portion of the farther contour and re-compute the plane of that contour based on the adjusted depths until the two folds no longer conflict.

Fig. 11(a) shows an example of reconstructed colon folds in 3D space. After interpolation between these folds to generate the wire-frame of the colon structure is completed (Fig. 11(b)), we divide the wire-frame into small polygons for smooth rendering using OpenGL. We render 40,000 (200 circumferential  $\times$  100 stacks  $\times$  2

triangles) polygons in between two folds to express smooth colon surface in our experiments.

### 3.3. Unobserved area calculation and visualization

We can use the reconstructed model for visualizing candidate areas that were not inspected by the endoscopist. It is not difficult to mark the unobserved area using OpenGL. Since camera lens and light source are at the same location, we just can render shadow on the virtual colon surface using stencil buffer. However, in this way, we cannot calculate the percentage of the unobserved area because OpenGL does not provide any method to tell which polygon shadow is rendered. Thus, we calculate the unobserved area as follows. For each polygon, we check three conditions: (i) if the polygon is facing the endoscope (the origin of the coordinate system), (ii) if the polygon is within the camera field-of-view, and (iii) if there are no obstacles from the polygon to the endoscope. The first condition is satisfied if the angle difference (in the range of [0–180]) between the normal of the polygon and the vector from the camera to the center of the polygon is greater than 90°. We call this vector to this polygon the *line of sight of the polygon*. The second condition is satisfied if the angle difference between the line of sight of the polygon and the camera direction is at most half of FOV of the camera. The last condition is satisfied if the distance of the polygon from the camera is same as the OpenGL-provided depth (Z-value) of the corresponding pixel in the viewport. Every pixel in a viewport has its own depth value indicating the distance of the closest object from the camera in that direction. When any of the three conditions is not satisfied, we count that polygon as an unobserved polygon. Therefore, we calculate the percentage of the unobserved mucosa area as the percentage of unobserved polygons. We render the unobserved polygons in green. See Fig. 11(c).

## 4. Experimental environment and results

We conducted quantitative evaluation of our technique using an Olympus synthetic colon model (Fig. 12(a)) and computed average deviations of fold depths and fold circumferences of the reconstructed models from the synthetic colon model. For qualitative evaluation, we selected thirty-eight images from different segments of the real colon from six screening colonoscopy procedures to show that our technique works on real colonoscopy images as well. The input image resolution was 720  $\times$  480 pixels. For displaying the virtual colon, we used the OpenGL default projection model (perspective projection) because OpenGL does not natively support the equidistance projection used in fish-eye lenses. Thus, a slight distortion and different depth perception is noticeable for some images.

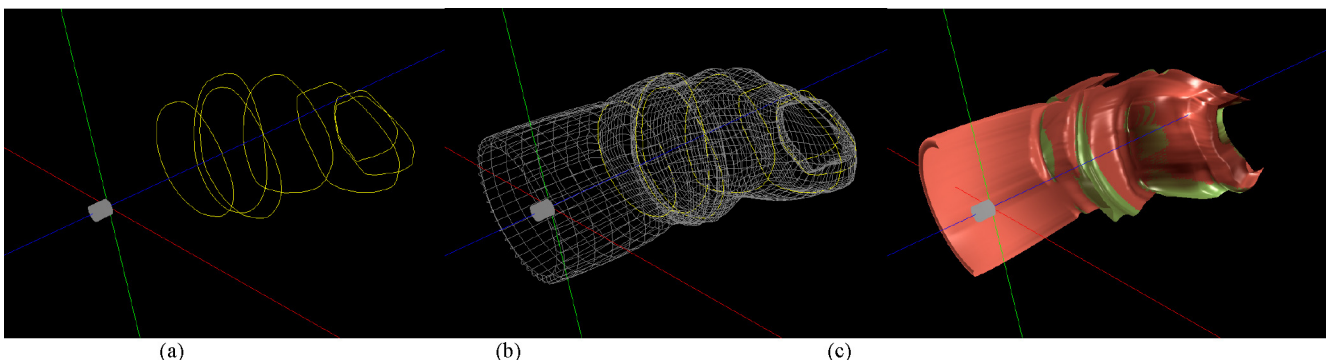


**Fig. 11.** (a) As a result of *DfI* algorithm in Section 3.1, fold contours are located in 3D space. (b) Wire-frame of a reconstructed colon segment after surface generation using OpenGL. (c) Half rendered virtual colon segment with unobserved areas shown in green.

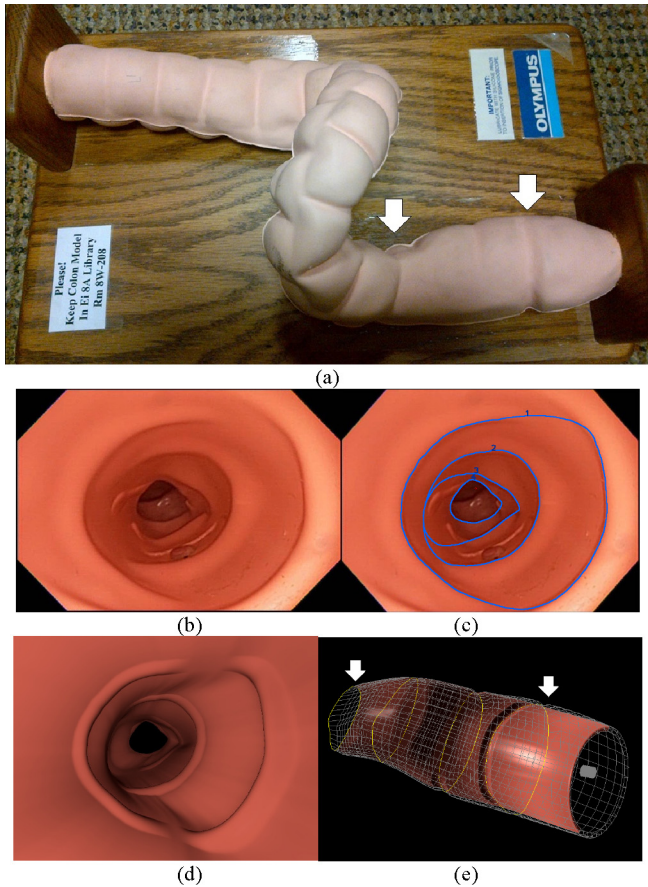


**Fig. 12.** (a) Olympus synthetic colon model. (b) Image (06990) taken by an endoscope camera inside the colon model in (a). (c) Image (b) superimposed with labeled fold contours in blue; the contours are numbered from 1 (the outermost contour) to 4 (the innermost contour). (d) Reconstruction result using the fold contours and Equation (5) with the brightness intensity calibration. (e) Side view of the half rendered reconstructed colon with the brightness intensity calibration. The section between the two white arrows in (e) corresponds to the section of the colon model between the two white arrows in (a). Overall shape of the two sections is similar and the left parts of these sections are narrower than the right parts.

**Table 1** shows parameter values used in our implementation. The values were determined based on experiments using a set of images not included in the image set for the evaluation in Section 4.2. FoV was set to  $110^\circ$  since image is cropped and the actual coverage was in fact  $110^\circ$  as observed during our experiments to determine the formula for brightness intensity calibration.

**Table 1**  
Parameters and default values.

Step	Parameter and value
Depth-from-Intensity (Section 3.1.2)	$C = 150$ $K = 10$ $T = 20$ $B = 15$ $FoV = 110$ $m = 1$
Colon surface generation (Section 3.2)	$P = 200$ $C_1 = 1/2$ $C_2 = 15$ $C_3 = 1/2$ $C_4 = 1/5$ $W = 0.005; H = 0.25$

**Table 2**

Depth represents the distance from the camera. Circf. represents the circumference. MAD is the mean absolute difference (error) between measurements taken from the ground truth and the reconstructed model using the default setting. The lower the MAD, the better the result.

	Ground truth (mm)		Reconstructed model		Absolute difference	
	Depth	Circf.	Depth	Circf.	Depth	Circf.
Fold 1	28	200	42	202	14	2
Fold 2	65	184	73	184	8	0
Fold 3	108	180	111	190	3	10
Fold 4	128	160	139	129	11	31
MAD					9	11

#### 4.1. Tests on an Olympus synthetic colon model

The picture of the synthetic colon model is shown in Fig. 12(a). The model has three sections: the straight beginning with the narrow end; the curve section in the middle, and the ending straight section. With the model, we measured outside distances between folds and outside fold circumference since measuring the inside circumference of the fold accurately is difficult. We used the information as ground truth for objective evaluation of the reconstruction algorithms. We picked four images from each section of the colon model. We selected these images since the fold contours in these images were detected well so that we can focus on evaluating the reconstruction results.

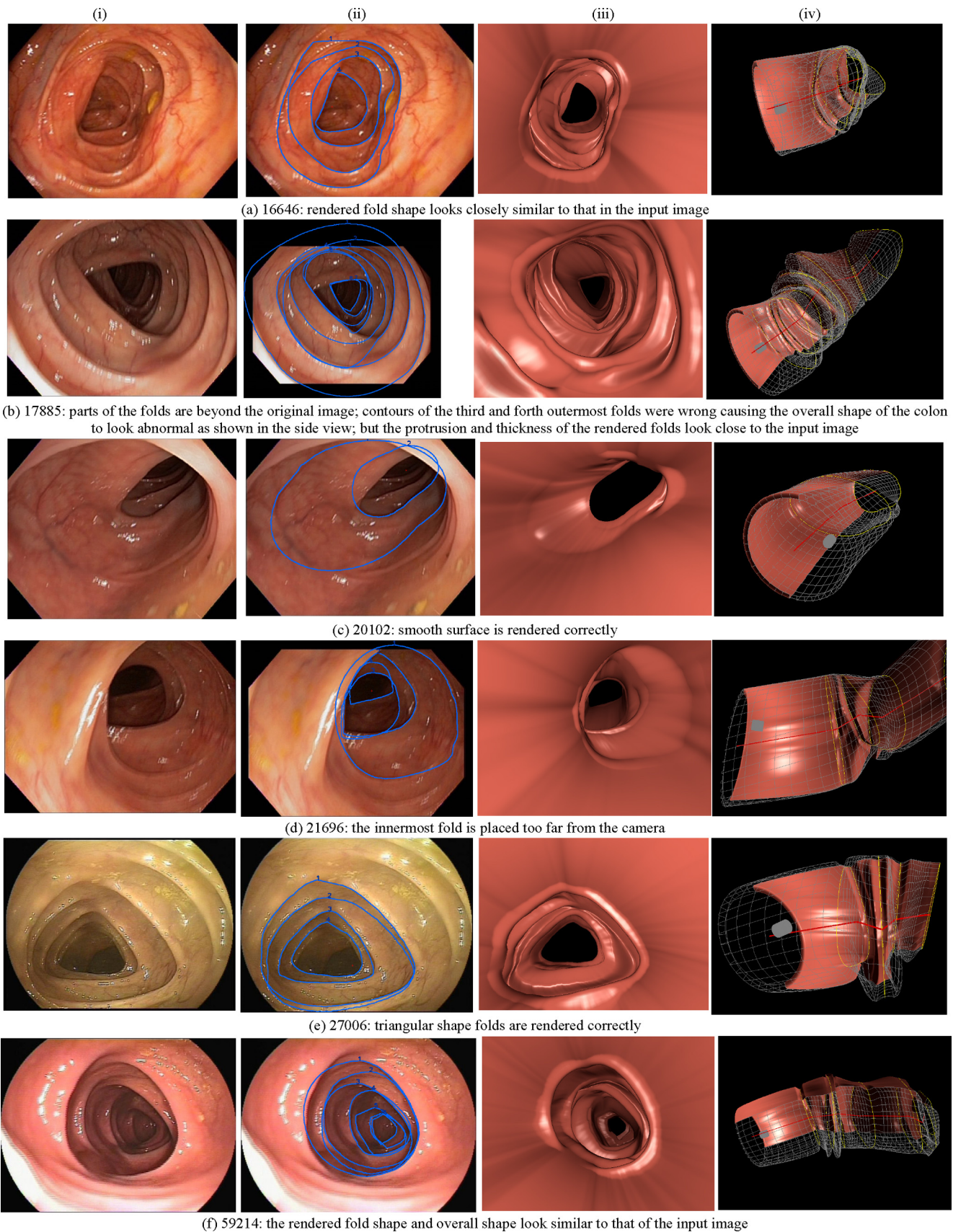
##### 4.1.1. Performance evaluation on the synthetic colon model

Fig. 12(a) is the picture of the model. Fig. 12(b) shows an image taken from the inside of the colon model. The detected contours are automatically labeled and shown in Fig. 12(c). Fig. 12(d) is the reconstruction result with the parameter values in Table 1. Comparing Fig. 12(b) and (d), the right part of the outermost fold, fold 1, is shown the generated colon with the highest amount of protrusion as shown in the input image (Fig. 12(b)). The left part of fold 1 in the virtual colon model is less protruded than the right part of fold 1. The upper and lower parts are flat as in the input image. Table 2 shows the ground truth of each fold as well as measurements taken from the virtual colon generated by our algorithm using Fig. 12(b). We scaled the reconstructed circumferences and depths using the same scale factor to match them to the same units. The scale factor was determined by matching the circumference of fold 2 of the virtual colon with the ground truth of fold 2. In this case, we used fold 2 to determine the scale factor since its shape is most similar to the real fold 2. The mean absolute difference (error) of the depth and the circumference are 9 and 11 mm, respectively.

Table 3 shows MAD for each image in different sections of the colon model. The average MAD for depth and circumference are computed using MADs of all twelve images. The average depth error is around 4 mm with the minimum depth error of only 1 mm. We observed that the folds were seen within the range of 20–150 mm from the camera. The average depth error of 4 mm is small compared to this range. The average circumference error is around 12 mm, which is less than 1/10 of the circumference of folds in the colon model (140–200 mm).

##### 4.1.2. Determination of suitable value of $m$ in Eq. (5)

Table 4 shows that the value  $m = 1$  gives the least error for both depth and circumference while  $m = 2$  (the original Lambert's cosine law) gives the highest error. The reason is that glossy colon surface causes ambient light as shown in Fig. 5b. Protruding folds can block some ambient light as illustrated in Fig. 5c. The amount of ambient light varies between images depending on the camera view angle and fold protrusion. For this image set,  $m = 1$  shows the least error.



**Fig. 13.** (i) Original input image. (ii) Automatically detected fold contours superimposed on the input image. (iii) Front view of the virtual colon. (iv) Side view of the half rendered virtual colon. (a) 16646: rendered fold shape looks closely similar to that in the input image; (b) 17885: parts of the folds are beyond the original image; contours of the third and forth outermost folds were wrong causing the overall shape of the colon to look abnormal as shown in the side view; but the protrusion and thickness of the rendered folds look close to the input image; (c) 20102: smooth surface is rendered correctly; (d) 21696: the innermost fold is placed too far from the camera; (e) 27006: triangular shape folds are rendered correctly; (f) 59214: the rendered fold shape and overall shape look similar to that of the input image.

**Table 3**

MAD in depth and MAD in circumferences of 4 images for each section.

	Image ID	Depth MAD	Circf. MAD
Section 1 Straight	06990	9	11
	00080	5	7
	13000	4	12
	07230	5	23
Section 2 Curve	00170	2	4
	00180	1	0
	00270	5	0
	00370	1	30
Section 3 Straight	15010	3	9
	16220	8	16
	15950	4	26
	02870	2	7
Average MAD		4.1	12.1

**Table 4**

Average estimation errors over twelve input images in Table 3 using different values of  $m$  in Eq. (5).

Average MAD of	0.5	0.75	1.0	1.25	2.0
Depth	13.3	8.5	4.1	8.2	30
Circf.	29.5	18.8	12.1	14.3	38.2

Future extension to include a well-studied formula that accurately estimates an amount of ambient light to Eq. (5) should give better results.

#### 4.1.3. Effectiveness of brightness intensity calibration

Table 5 shows that with intensity calibration (Section 3.1.1), the error is lower for both depth and circumference estimates.

#### 4.2. Tests on real colons

We evaluated the proposed reconstruction technique objectively in terms of overall shape of reconstructed models with the synthetic colon. In this section, we evaluate our technique qualitatively about how well fold shapes are expressed with real colons since we could not measure fold protrusion (height) and thickness (width) inside the real colon. Moreover, we cannot obtain the ground truth shape of real colons even with CT data since the positions of the patient during CT colonography and colonoscopy are different, and the colon is not rigid. However, we can feel the amount of protrusion and thickness of folds when looking at them in 2D images. We can qualitatively compare how similar protrusion and thickness by looking at the images of the inside of the real colon and the rendered reconstructed models under the same view direction and distance.

Six cases are shown in Fig. 13. The original input images are shown in the first column of Fig. 13. The second column shows the corresponding input images overlaid with automatically detected fold contours. In the third column, front views of virtual colons reconstructed by the proposed algorithm are presented. Side views of the half rendered virtual colons are displayed in the fourth column.

**Table 5**

Effectiveness of intensity calibration on reconstructed results over twelve input images in Table 3.

Average MAD of	w/intensity calibration	w/o intensity calibration
Depth	4.1	6.8
Circf.	12.1	15.2

**Table 6**

Execution time per module.

	Execution time (s)
Depth estimation	0.008
Surface generation	0.016
Polygon construction	0.075
Unobserved area calculation	0.128
Total	0.227

#### 4.3. Average execution time per image

We ran our reconstruction software given the fold contours on a 64-bit Windows 7 workstation with Intel Xeon E5504 CPU (two 2.0 GHz processors) and 6 GB of RAM. Table 6 shows the time taken for each key step of the colon reconstruction techniques. The most time consuming step is unobserved area calculation.

#### 4.4. Discussion

We have shown the effectiveness of our intensity calibration in lowering the error of fold depth and circumference. Our modification of the Lambertian cosine law is effective. Our method for estimating fold protrusion and thickness is promising since it expresses flat surface and protruded surface effectively for most images we observed in our data set. The quality of the 3D reconstruction result largely depends on the result of contour estimation. Good contour estimation gives good 3D reconstruction results with low depth and circumference estimation errors as demonstrated in Tables 2 and 3. We observed more errors on folds far from the camera because of occlusion. The reconstruction time is quite fast. The depth estimation process is fast (less than 8 ms as shown in Table 6) and can be done in real-time. The results are stored and later used for the calculation and visualization of the unobserved areas. This step is only done on request of the endoscopist when ready to see the feedback. Despite the promising result, our data set is limited due to the limitation of the ground truth of the synthetic colon model. Furthermore, 3D ground truth data of the real colon during colonoscopy while the patient is lying sideways is not available. Obtaining such ground truth is difficult if not impossible using current equipment and practice.

#### 5. Conclusion and future work

In this paper, we present our new depth from intensity 3D reconstruction technique of a colon structure. We use intensity calibration to handle uneven distribution of light rays on colon surface. We found that ambient light affects the relationship between brightness intensity and distance of colon surface from the camera described by the Lambertian's cosine law. We proposed a modification of the Lambertian's cosine law and showed the effectiveness of our modification. Our technique is the first fully automated technique that reconstructs a colon structure with fold protrusion and thickness from a 2D colonoscopy image. Most other existing works reconstruct the colon surface. Our reconstructed colon structures from images of real colons are quite good in terms of expressing fold protrusion and fold thickness. Our proposed work and findings provide insights into the complexity of this very challenging problem and provide the basis for further studies.

Our future work is to construct better ground truth by building our own synthetic colon model in consultation with the domain experts. In parallel, we will develop an algorithm that tracks fold edges in a sequence of images and combines reconstructed colons from the image sequence to form a single more reliable colon model. This process provides camera motions (forward/backward movement, rotation, and tilting), which can

be used to retrospectively simulate camera movement on the reconstructed virtual colon to label candidate areas unseen by the endoscopist. Since blurred images and fast camera movement can result in lost tracking, we will investigate an effective algorithm to combine consecutive reconstructed models together using partial 3D object similarity. These functionalities will be added to our SAPPHIRE middleware that enables real-time capturing of endoscopy video frames, real-time analyses, and feedback [42]. We envision that the endoscopist can ask for the 3D map showing inspection at the end of each major colon section (right colon, transverse colon, and left colon). Hence, our software will run polygon surface construction and visualization on-demand only. The endoscopist can revisit the unseen area reported by the software for each colon segment to improve polyp detection yields. Finally, we will evaluate how well the software helps to improve quality of colonoscopy in a clinical trial. To realize this vision, we need to solve a number of challenging questions.

### Conflict of interest statement

Wong, Tavanapong, and Oh have management roles and own stock in EndoMetric Corp. Piet de Groen and Mayo Clinic have a financial interest and hold an equity position in EndoMetric Corp, a company that analyzes colonoscopy video streams for features of quality.

### Acknowledgements

This work was supported in part by the National Science Foundation STTR Grant No. IIP-0956847, Agency for Healthcare Research and Quality Grant No. HS17537, National Institute of Diabetes and Digestive and Kidney Diseases Grant No. DK083745, Mayo Clinic, and EndoMetric Corporation. Opinions and findings in this paper are those of the authors and do not represent those of the funding agencies.

### References

- [1] American Cancer Society. Colorectal cancer facts & figures; 2012.
- [2] Brenner H, Hoffmeister M, Arndt V, Stegmaier C, Altenhofen L, Haug U. Protection from right- and left-sided colorectal neoplasms after colonoscopy: population-based study. *J Natl Cancer Inst* 2010;102(2):89–95.
- [3] Baxter N, Goldwasser M, Paszat L, Saskin R, Urbach D, Rabeneck L. Association of colonoscopy and death from colorectal cancer. *Ann Intern Med* 2009;150(1):1–8.
- [4] Hewett DG, Kahi CJ, Rex DK. Does colonoscopy work? *J Natl Compr Canc Netw* 2010;8(1):67–76.
- [5] Gupta, R, Steinbach, M, Ballman, KV, Kumar, V, de Groen, PC. Colorectal cancer despite colonoscopy: critical is the endoscopist, not the withdrawal time. Digestive disease week 2009, Chicago, IL, USA.
- [6] De Groen PC. Advanced systems to assess colonoscopy. *Gastrointest Endosc Clin N Am* 2010;20(4):699–716.
- [7] Eddakanambeth, VJ, Enders, F, Tavanapong, W, Oh, J, Wong, J, de Groen, PC. Colonoscopy what endoscopists inspect under optimal conditions. Digestive disease week 2011, Chicago, IL, USA.
- [8] Hong D, Tavanapong W, Wong J, Oh J, de Groen PC. 3D Reconstruction of colon segments from colonoscopy images. In: Proc. of IEEE int'l conf. on bioinformatics and biengineering. 2009. p. 53–60.
- [9] Deguchi K. Shape reconstruction from endoscope image by its shadings. In: Proc. of IEEE/SICE/RSJ int'l conf. on multisensor fusion and integration for intelligent systems. 1996. p. 321–8.
- [10] Koppel D, Chen C, Wang Y, Lee H, Gu J, Poirson A, Wolters R. Toward automated model building from video in computer-assisted diagnoses in colonoscopy. In: Proc. of SPIE medical imaging conference. 2007.
- [11] Kaufman A, Wang J. 3D surface reconstruction from endoscopic videos. visualization in medicine and life sciences, mathematics and visualization; 2008. p. 61–74.
- [12] Hong D, Tavanapong W, Oh J, Wong J, de Groen PC. A new technology to visualize what the endoscopist does not see during colonoscopy. Digestive disease week 2009. Chicago, USA: McCormic Place; 2009.
- [13] Hong D, Tavanapong W, Wong J, Oh J, de Groen PC. Colon fold contour estimation for 3D visualization of colon structure from 2D colonoscopy images. In: Proc. of IEEE int'l symp. on biomedical imaging: from nano to macro. 2011. p. 121–4.
- [14] Summers RM, Johnson CD, Pusanik LM, Malley JD, Youssef AM, Reed JE. Automatic polyp detector for CT colonography: feasibility study in a human population. *Radiology* 2001;219(1):51–9.
- [15] Yoshida H, Masutani Y, MacEneaney P, Rubin DT, Dachman AH. Computerized detection of colonic polyps at CT colonography on the basis of volumetric features: pilot study. *Radiology* 2002;222(2):327–36.
- [16] Gokturk SB, Tomasi C, Acar B, Beaulieu CF, Paik D, Jeffrey RB, Yee J, Napel SA. Statistical 3D pattern processing method for computer-aided detection of polyps in CT colonography. *IEEE Trans Med Imaging* 2001;20(12):1251–60.
- [17] Zhao L, Botha CP, Besscos JV, Tryoen R, Vos FM, Post FH. Lines of curvature for polyp detection in virtual colonoscopy. *IEEE Trans Vis Comput Graph* 2006;12(5):885–92.
- [18] Li P, Napel S, Acar B, Paik DS, Jeffrey RB, Beaulieu CF. Registration of central paths and colonic polyps between supine and prone scans in computed tomography colonography: pilot study. *Med Phys* 2004;31(10):2912–23.
- [19] Zeng W, Marino J, Chaitanya K, Xianfeng DG, Kaufman AE. Supine and prone colon registration using quasi-conformal mapping. *IEEE Trans Vis Comput Graph* 2010;16(6):1348–57.
- [20] Lakare S, Chen D, Li L, Kaufman A, Liang Z. Electronic colon cleansing using segmentation rays for virtual colonoscopy. In: Proc. of SPIE medical imaging. 2002. p. 412–8.
- [21] Zalis M, Perumpillichira J, Hahn P. Digital subtraction bowel cleansing for CT colonography using morphological and linear filtration methods. *IEEE Trans Med Imaging* 2004;23(12):1335–43.
- [22] Li L, Wang S, Wang J, Eremina D, Wei X, Liang Z. A new electronic colon cleansing method for virtual colonoscopy. In: Proc. of SPIE medical imaging 2007: physiology, function, and structure from medical images, vol. 6511. 2007.
- [23] Liang Z, Wang S. An EM approach to MAP solution of segmenting tissue mixtures: a numerical analysis. *IEEE Trans Med Imaging* 2009;28(2):297–310.
- [24] Halier S, Angement S, Tannenbaum A, Kikinis R. Nondistorting flattening maps and the 3D visualization of colon CT images. *IEEE Trans Med Imaging* 2000;19(7):665–70.
- [25] Huang A, Roy D, Franaszek M, Summers RM. *Teniae coli* guided navigation and registration for virtual colonoscopy. In: Proc. of IEEE visualization. 2005. p. 279–85.
- [26] Marino J, Qiu F, Kaufman A. Registration of virtual and optical colonoscopy views. In: Proc. of MICCAI 2008 workshop: computational and visualization challenges in the new era of virtual colonoscopy. 2008. p. 122–6.
- [27] Marino J, Qiu F, Kaufman A. Virtually assisted optical colonoscopy. In: Proc. of SPIE medical imaging 2008: physiology, function, and structure from medical images, 2008, vol. 6916 69160J-1. 2008.
- [28] Cohen L, Vinet L, Sander PT, Gagalowicz A. Hierarchical region based stereo matching. In: Proc. of IEEE conf. on computer vision and pattern recognition (CVPR). 1989. p. 416–21.
- [29] Scharstein D, Szeliski R. A taxonomy and evaluation of dense two-frame stereo correspondence algorithms. *Int J Comput Vis* 2002;2002(47):7–42.
- [30] Forsyth DA. Shape from texture without boundaries. In: Proc. of European conf. on computer vision, vol. 2002. 2002. p. 225–39.
- [31] Prados E, Faugeras O. Shape from shading: a well-posed problem? Proc. of IEEE conf. on computer vision and pattern recognition. 2005. p. 870–7.
- [32] Zhang R, Tsai PS, Cryer JE, Shah M. Shape-from-shading: a survey. *IEEE Trans Pattern Anal Mach Intell* 1999;21(8):690–706.
- [33] Tomasi C, Kanade T. Shape and Motion from Image Streams: Factorization Method (Full Report on the Orthographic Case). Carnegie Mellon University Technical Report CMU-CS-91-132; 1991.
- [34] Zhou J, Das A, Li F, Li B. Circular generalized cylinder fitting for 3D reconstruction in endoscopic imaging based on MRF. In: Proc. of computer vision and pattern recognition workshops. 2008. p. 1–8.
- [35] Suri JS, Singh S, Laxminarayana S, Zeng X, Liu K, Reden L. Shape recovery algorithms using level sets in 2D/3D medical imagery: a state-of-the-art review. *IEEE Trans Inform Technol Biomed* 2002;6(1):8–28.
- [36] Shi J, Malik J. Normalized cuts and image segmentation. *IEEE Trans Pattern Anal Mach Intell* 2000;22(8):888–905.
- [37] Boykov YY, Jolly MP. Interactive graph cuts for optimal boundary and region segmentation of objects in N-D images. In: Proc. of int'l conf. on computer vision, vol. 1. 2001. p. 105–12.
- [38] Bakstein H, Pajdla T. Panoramic mosaicing with a 180° field of view lens. In: Proc. of IEEE workshop on omnidirectional vision. 2002. p. 60–8.
- [39] Kannala J, Brandt S. A generic camera calibration method for fish-eye lenses. In: Proc. of IEEE int'l conf. on pattern recognition. 2004. p. 10–3.
- [40] Lutus, P. Polynomial regression data fit. <http://www.arachnoid.com/polysolve/index.html>. 2011.
- [41] Sederberg, T. Bézier curves. <http://www.tsplines.com/resources/class.notes/Bezier.curves.pdf>. 2011.
- [42] Stanek SR, Tavanapong W, Wong J, Oh J, Nawarathna R, Muthukudag J, de Groen PC. SAPPHIRE middleware and software development kit for medical video analysis. In: Proc. of IEEE int'l symp. on computer-based medical systems. 2011.